applied sciences

MDPI

Article

A Performance Test and Internal Flow Field Simulation of a Vortex Pump

Ping Tan [1], Yi Sha [1,*], Xiaobang Bai [2], Dongming Tu [1], Jien Ma [3,4,5,*], Wenjun Huang [3,4,5] and Youtong Fang [3,4,5]

1 School of Automation and Electrical Engineering/ School of Mechanical & Automotive Engineering, Zhejiang University of Science and Technology, Hangzhou 310023, China; tankor@zju.edu.cn (P.T.); 221601852001@zust.edu.cn (D.T.)
2 College of Energy and Power Engineering, Lanzhou University of Technology, Lanzhou 730050, China; baixiaobang@163.com
3 College of Control Science and Engineering, Zhejiang University, Hangzhou 310027, China; huangwj@supcon.com (W.H.); youtong@zju.edu.cn (Y.F.)
4 College of Electrical Engineering, Zhejiang University, Hangzhou 310027, China
5 China Academy of West Region Development, Zhejiang University, Hangzhou 310027, China
* Correspondence: Shayi01@sina.com (Y.S.); jienma@126.com (J.M.)

Received: 17 September 2017; Accepted: 1 December 2017; Published: 7 December 2017

Abstract: Vortex pumps have good non-clogging performance and are widely used in the fluid transportation of food, sewage treatment, and mineral and coal slurry transportation. In order to design and manufacture a vortex pump with good performance and establish a method of optimum design, we must master the internal flow rules of the pump. Based on the self-design vortex pump (32WB8-12) experiment, the discharge-pump head (q_v-H), discharge-pump shaft power (q_v-P), discharge-pump efficiency (q_v-η), and discharge-critical net positive suction head (q_v-$NPSH_c$) curves are obtained, and the q_v-$NPSH_c$ curve shows an opposite tendency compared with the centrifugal pump. With the mathematical model selected with respect to the optimal condition, the three-dimensional internal flow within the vortex pump has been numerically simulated by a renormalization group k-ε (RNG k-ε) turbulence model. The static pressure (p_s) and velocity distribution of the impeller and the middle section of the volute at 0°, 90°, 180°, and 270° are obtained, and the performance curves have been fitted using a CFX-calculated energy parameter. It was illustrated that the velocity field is relatively disordered and the flow in the impeller region is of a forced vortex character. The flow in the volute is similar to that of the combined vortex with backflow, which is a non-axisymmetric unsteady flow with quite high turbulence intensity. These factors are the main reasons for the relatively low efficiency of the vortex pump. The measurement of flow field in volute with a five-hole probe was conducted, and it is demonstrated that the numerical results are in good agreement with the flow field measurement data. An upward pressure gradient forms in the portal area of the impeller, and it is confirmed that the lowest pressure point is located in the upper position of the impeller hub. It is revealed that for the vortex pump to have advanced suction and anti-cavitation performance, the lowest pressure in the pump should be -4×10^4 Pa and it should be located at the center of the vortex chamber cavity.

Keywords: vortex pump; computational fluid dynamics (CFD); five-hole spherical probe; *NPSH*

1. Introduction

The vortex pump evolved from a centrifugal pump with a semi-open impeller, and it is a type of non-clogging pump with an impeller located completely within the impeller chamber behind the vortex chamber, as shown in Figure 1. Its unique structure makes it suitable for conveying

solid–liquid mixtures containing solid and long fibers [1–3], and in particular, it shows excellent performance in the hydraulic transportation of gases containing manure, biogas, digesters, waste liquid, and agricultural products such as potato, etc., whilst solid media were not damaged. At present, if we compare the vortex pump with the centrifugal pump, the biggest disadvantage is the low efficiency of the vortex pump [4,5]. In recent years, researchers have carried out studies on pump design and numerical simulation to improve the performance of the vortex pump. Gerlach et al. analyzed the how variations in geometric parameters influence vortex pump characteristics, and investigated many articles considering parameters in both single-parameter and multi-parameter experiments [6,7]. Moreover, Gerlach et al. performed a numerical study of the internal flow field of a vortex pump, and made a comparison with the Hamel–Oseen vortex model. The study suggests that a vortex similar to the Hamel–Oseen vortex is only present at the strong part load operation [8]. Through a numerical simulation and experimental analysis, Jiang and Zhu studied the influence of different types of hems and blades on the performance of the vortex pump [9,10]. Li carried out a numerical simulation and experiment analysis for the gas–liquid two-phase vortex pump [11]. Because of the change in structure from a centrifugal pump to a vortex pump, the internal flow of the vortex pump is complicated, and the flow through the outlet of the pump is the intersection of the flow through the vortex chamber and the impeller. The 32WB8-12 vortex pump was built based on continuous research findings from the 1980s. In order to design and manufacture a vortex pump with good performance and establish a method of optimum design, we must master the internal flow rules of the pump. So, this paper carries out research work on a performance test and internal flow field simulation of the vortex pump. At present, the internal flow velocity field of the vortex pump can be measured by the particle image velocimetry (PIV) technique, but the pressure field of the high-speed rotating impeller cannot be measured without contact. Therefore, the numerical calculation of the flow field is an effective way to obtain the internal flow rules. In order to determine whether the calculation results are correct and can reflect the actual objective, we need scientific experimental verification. The volute chamber of the vortex pump is relatively wide, so it is possible to measure the flow field by probe contact. As long as verification of the numerical calculation results of the vortex chamber flow field through comparative analysis reaches a certain level of precision, it can be extended to deduce that the numerical calculation of the internal flow field of the whole vortex pump gives realistic results. Our paper is based on this idea.

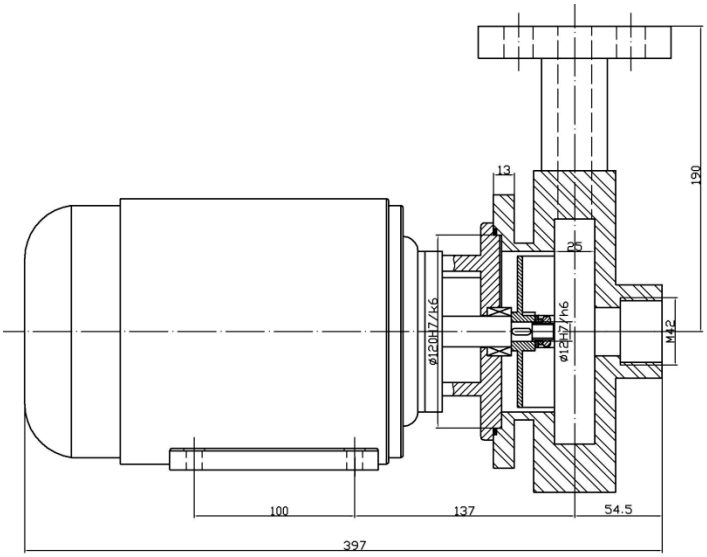

(**a**)

Figure 1. *Cont.*

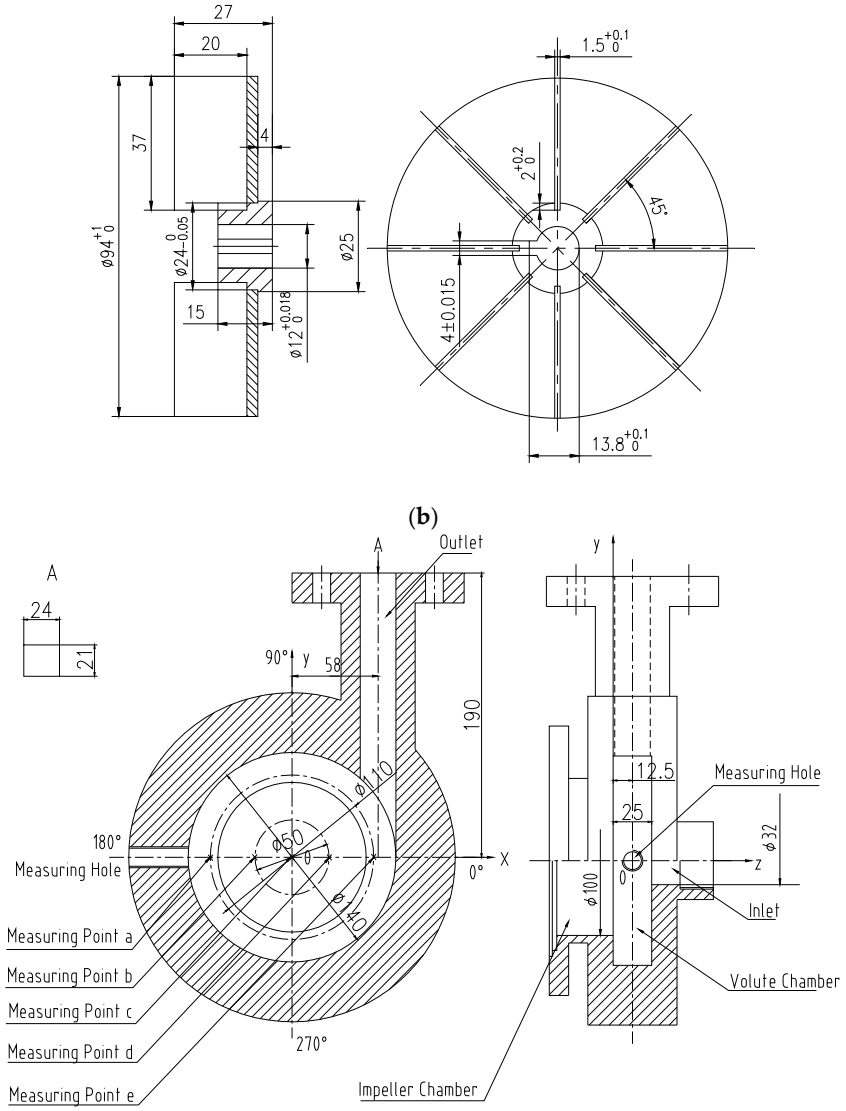

Figure 1. Structure and distribution of the hydraulic geometric sketch. (**a**) Structure diagram of the vortex pump; (**b**) Impeller component and geometric parameters; (**c**) Chamber component and geometric parameters.

The flow field inside the vortex pump was simulated by ANSYS® CFX software, and the performance curve was calculated based on the design, development, and performance test of the model pump. The flow field in the vortex chamber was measured by a five-hole probe, and the correctness of the numerical results was verified. After a comprehensive analysis, the internal flow rules of the vortex pump and the constraint relationship between the pump performance and the flow characteristics were clarified.

2. Design and Test Scheme of the Model Pump

For the study of the vortex pump, considering factors such as the scale of the test platform, this paper designed and developed the 32WB8-12 pump (Zhejiang University of Science and Technology, Hangzhou, Zhejiang, China) model. The hydraulic design and geometric parameters are shown in Table 1, and its structure and impeller, pressurized water chamber parts, coordinate system, and the position of the measuring hole are shown in Figure 1.

Table 1. Vortex pump design and hydraulic parameters.

Design Parameters		Hydraulic and Geometric Parameters			
Discharge/q_v (m^3/h)	9	Specific speed/n_s	80.67	Diameters of impeller/D_2 (mm)	94
Head/H (m)	12	Chamber diameter/D_V (mm)	140	Chamber throat area/F_{thr} (mm^2)	504
Rotational speed/n (r/min)	2850	Width of blade/b_2 (mm)	20	Width of chamber (mm)	25
Pump efficiency/η (%)	50	Volute chamber lines	ring-shaped	Base circle diameter of chamber/D_3 (mm)	100
Shaft power/P (kW)	0.55	Number of blades/Z (piece)	8	Diameter of volute/D_j (mm)	32
Net positive suction head/$NPSH_r$ (m)	4	Blade thickness/δ (mm)	1.5	Blade airfoil lines	radialized

3. Model Pump Performance

The pump is directly connected to the motor, and the power of the pump shaft was measured by the electronic method. The no-load motor is in line with GB/T 12785-91 standards (Test Methods for Submersible Motor Pumps), the pump performance test was carried out according to GB/T 3216-2005 (Rotodynamic Pumps—Hydraulic Performance Acceptance Tests, Grades 1 and 2), and the frequency converter was used to adjust to the rated speed. Figure 2 is the scheme of the experimental test bench. The technical data for instrumentation are provided in Table 2.

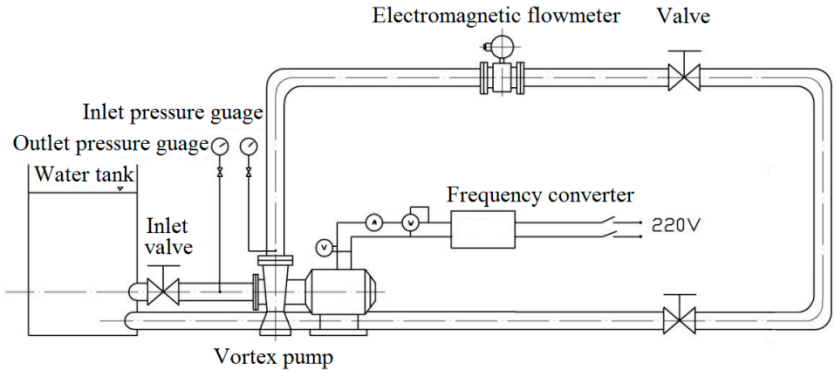

Figure 2. Scheme of the experimental test bench.

Table 2. The technical data for instrumentation.

Parameter	Instrument	Precision	Parameter	Parameter	Precision
Pump head/H	pressure gauge	0.4	Current/A	ammeter	0.5
	vacuum gauge	0.4	Voltage/V	voltmeter	0.5
Discharge/q_v	electromagnetic flow meter	0.5	Shaft power/P	wattmeter	0.5
Rotation rate/n	digital tachometer	0.5	Resistance/R	digital resistance meter	0.1

Pump experimental performance curves are shown in Figure 3 (η_{gr} is the unit efficiency). The optimal operating conditions of the pump are: discharge (q_v) is 9.00 m^3/h, pump head (H) is 12.88 m, maximum efficiency (η_{max}) is 53.13%, and specific speed n_s is 76.5. The pump q_v-H curve is flat, higher than in the design condition. The q_v-P curve rises faster than other curves. The discharge-critical net positive suction head (q_v-$NPSH_c$) curve is parabolic-diminishing and shows the opposite trend compared with the centrifugal pump's q_v-$NPSH_c$ curve. The critical $NPSH$ of small flow is larger, but the critical $NPSH_c$ decreases with the increased discharge.

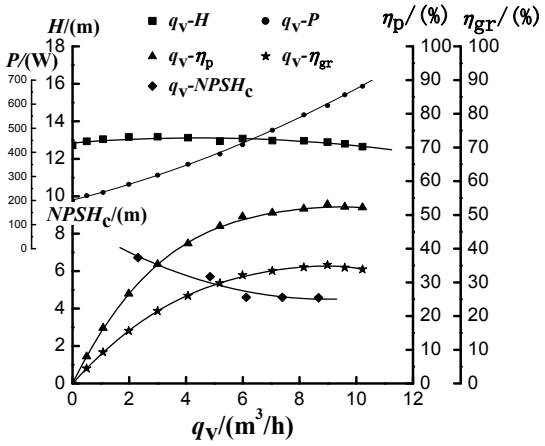

Figure 3. Experimental pump performance curves.

η_p: pump efficiency; η_{gr}: unit efficiency; H: pump head in m; P: shaft power in W; $NPSH_c$: critical net positive suction head in m; q_v: discharge in m^3/h; q_v-H: discharge-pump head; q_v-P: discharge-pump shaft power in w; q_v-η_p: discharge-pump efficiency; q_v-η_{gr}: discharge–unit efficiency; q_v-$NPSH_c$: discharge-critical net positive suction head.

4. Numerical Calculation of Pump's Internal Flow Field

4.1. Governing Equation

The flow field was calculated based on selecting the best condition of pump performance test. The internal flow field of the vortex pump is very complex, which is three-dimensional turbulent flow dominated by strong swirling flow. It is affected by many factors, such as curvature, rotation, and so on. Choosing the turbulence model for the calculation of the internal flow field is very important. The previous calculation used the standard k-ε two-equation model [12–14], which is a local equilibrium model that cannot accurately predict turbulence with drastic changes in mean flow, such as separation flow and swirling flow. Later, the researchers applied the modified k-ε and the Reynolds stress equation model—which was derived from the anisotropic conditions—to the numerical calculation of the strong cyclonic flow field. The renormalization group k-ε turbulence model is called the RNG k-ε model. The coefficient in the RNG k-ε turbulence model is derived by using the RNG model theory. There is an additional item R in the k-ε equation, which represents the effect of the average strain rate on the turbulent dissipation rate ε. The RNG k-ε turbulence model can simulate the flow separation and vortex well. Moreover, because of the complexity of the Reynolds stress model and the large amount of computational resources, we chose the RNG k-ε model to numerically calculate the three-dimensional flow in the vortex pump [15].

There are three expressions of the governing equation:

(1) The continuity equation

$$\frac{\partial \rho}{\partial t} + \frac{\partial(\rho\overline{u_i})}{\partial x_i} = 0 \tag{1}$$

(2) The momentum equations

$$\frac{\partial(\rho\overline{u_i})}{\partial t} + \frac{\partial(\rho\overline{u_i u_j})}{\partial x_j} = -\frac{\partial \overline{p}}{\partial x_i} + \frac{\partial}{\partial x_j}\left[\mu\frac{\partial \overline{u_i}}{\partial x_j} - \rho\overline{u_i' u_j'}\right] \tag{2}$$

$$-\rho\overline{u_i' u_j'} = \mu_t\left[\frac{\partial \overline{u_i}}{\partial x_j} + \frac{\delta \overline{u_j}}{\delta x_i}\right] - \frac{2}{3}\left[\rho k + \mu_t\frac{\delta \overline{u_j}}{\delta x_i}\right]\delta_{ij} \tag{3}$$

(3) The k and ε equation

$$\rho\frac{Dk}{Dt} = \frac{\partial}{\partial x_j}\left[\left(\mu + \frac{\mu_t}{\sigma_k}\right)\frac{\partial k}{\partial x_j}\right] + 2\mu_t\overline{S_{ij}}\frac{\partial\overline{u_i}}{\partial x_j} - \rho\varepsilon \tag{4}$$

$$\rho\frac{D\varepsilon}{Dt} = \frac{\partial}{\partial x_j}\left[\left(\mu + \frac{\mu_t}{\sigma_\varepsilon}\right)\frac{\partial \varepsilon}{\partial x_j}\right] + 2C_{1\varepsilon}\frac{\varepsilon}{k}\mu_t\overline{S_{ij}}\frac{\partial\overline{u_i}}{\partial x_j} - C^*_{2\varepsilon}\rho\frac{\varepsilon^2}{k} \tag{5}$$

where

$$\mu_t = C_\mu\frac{k^2}{\varepsilon} \tag{7}$$

$$S_{ij} = \frac{1}{2}\left(\frac{\partial\overline{u_i}}{\partial x_j} + \frac{\delta\overline{u_j}}{\delta x_i}\right) \tag{8}$$

$$C^*_{2\varepsilon} = C_{2\varepsilon} + \frac{C_\mu\eta^3\left(\frac{1-\eta}{\eta_0}\right)}{1+\beta\eta^3} \tag{9}$$

$$\eta = \sqrt{2\overline{S_{ij}S_{ij}}}\frac{k}{\varepsilon} \tag{10}$$

where δ_{ij} is unit tensor, $\eta_0 = 4.38$, $C_\mu = 0.0845$, $\beta = 0.012$, $C_{1\varepsilon} = 1.42$, $C_{2\varepsilon} = 1.68$, $\alpha_k = 0.7194$, and $\alpha_\varepsilon = 0.7194$.

The environment temperature is 25 °C. The medium is water, and the density ρ is 997 kg/m^3. The dynamic viscosity μ is 0.89 mPa·s. The quantities with over-bar (such as $\overline{u_i}$) are mean values.

4.2. 3D Modeling and Grid Division

The 3D modeling software Pro/ENGINEER (Version 5.0, PTC, Needham, MA, USA, 2015) [16–19] was used to perform solid modeling of the vortex chamber of the vortex pump and impeller region. The computational domain consists of the impeller region and volute region, in which the volute region is the stationary region. The impeller region is the rotating region and the transmission coupling flow parameter between the impeller and volute region is processed by the frozen rotor method. The calculation of the impeller flow field is carried out in the relative coordinate system, while the vortex chamber flow field calculation is carried out in the absolute coordinate system and the integral calculation of the dynamic and static components is realized through the coupling calculations between the two parts. Because the interface grid between the computational domains is not exactly the same, the general grid interfaces (GGIs) are used to connect the parts. The computational grids are divided by ANSYS® ICEM Tetra tools (Version 14.5, ANSYS, Canonsburg, PA, USA, 2012). The tetrahedral mesh is divided into the vortex chamber region and the impeller region, respectively, and the residual error is 10^{-4}. The number of mesh units is 616,369, and the number of nodes is 117,300, as shown in Figure 4.

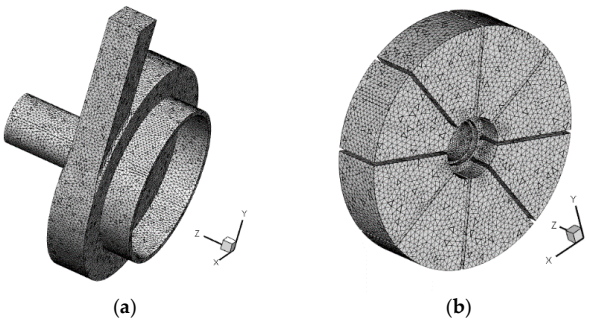

(**a**) (**b**)

Figure 4. Simulation grids: (**a**) Volute; (**b**) Impeller.

4.3. Boundary Conditions

4.3.1. Inlet Boundary Conditions

The inlet of the vortex pump calculation area is an axial inlet. The inlet axial velocity value is given at the inlet pipe according to the flow rate. Assuming that the inlet has no rotation, the tangential velocity and the radial velocity are 0, and the turbulence is fully developed and evenly distributed in the import section. A is the area of the inlet of the vortex pump. The inlet axial velocity v_{in} is given at the inlet pipe according to the flow rate q_v.

$$v_{in} = \frac{q_v}{A} \tag{11}$$

The turbulent kinetic energy and turbulent energy dissipation rate at the inlet are set according to the flow and inlet cross-sectional area. The formula is as follows:

$$k_{in} = \frac{3}{2}(\overline{u}I)^2 \tag{12}$$

$\overline{u}$ is the mean flow velocity, and here $\overline{u} = v_{in}$.

$$\varepsilon_{in} = C_{\mu}^{\frac{3}{4}} \frac{k_{in}^{\frac{3}{2}}}{l} \tag{13}$$

where I is turbulence intensity

$$I = u'/\overline{u} = 0.16\left(Re_{D_H}\right)^{-\frac{1}{8}} \tag{14}$$

From the above formula, u' is the root-mean-square of the turbulent velocity fluctuations, $\overline{u}$ is the is the mean velocity, and l is the inlet's length, Re_{D_H} is the Reynolds number based on D_H, and D_H represents the hydraulic diameter,

$$l = 0.07L \tag{15}$$

where C_{μ} is 0.09, and L is the associated length. For the full development of the turbulence, desirable L is equal to the hydraulzic diameter. Here, L is equal to the inlet round pipe diameter.

Specific boundary conditions: velocity vector (0 m/s, 0 m/s, 3.11 m/s), turbulent kinetic energy k_{in} = 0.021 m^2/s^2, and turbulent kinetic energy dissipation ε_{in} = 0.22 m^2/s^3.

4.3.2. Outlet Boundary Conditions

Assuming that the outlet flow is fully developed for turbulence, the specific boundary conditions are as follows:

The outlet type is known as Outlet, and the average static pressure p_s = 101,325 Pa.

4.3.3. Wall Boundary Conditions

In the non-slip boundary condition (No Slip) of the solid wall, the wall function method is used to calculate the turbulence in the vicinity of the wall. The influence of the wall roughness on the flow field is neglected in the calculation.

5. Numerical Results

5.1. The Flow Distribution of the Static Pressure Inside the Pump

Figures 5–8 are all based on the calculation result of CFX software (Version 14.5, ANSYS, Canonsburg, PA, USA, 2012). Based on the coordinate system in Figure 1, Figure 5 shows the static pressure distribution on the axial cross-section where Z is −10 mm. This axial section is also the middle cross-section of the impeller blade. According to the static pressure value and its position (radial

direction and $r = \sqrt{x^2 + y^2}$), Figure 6 is generated. Figure 6 shows the static pressure p_s variable curves along the 0°, 90°, 180°, and 270° radial directions. Figures 5 and 6 show that the center of the impeller is the lowest static pressure area in this axial cross-section, which is negative pressure (vacuum). The pressure in the center of the impeller is also lower than the pressure in the center of the chamber, so the run-through flow from chamber to impeller can be formed. When the fluid flow enters into the region near the blade, centrifugal force applies work on fluid flow and the pressure is increasing. So, in the region near the impeller edge, the pressure is higher than other regions.

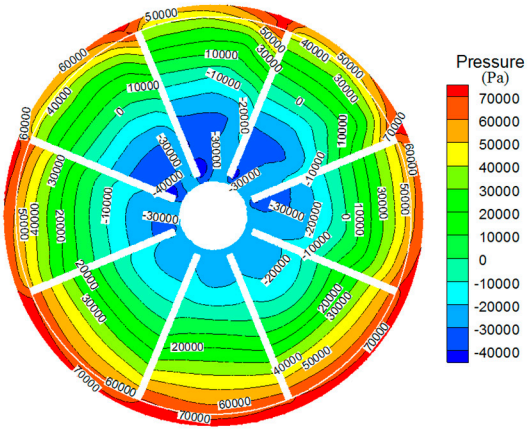

Figure 5. Static pressure distribution for the axial cross-section $Z = -10$ mm.

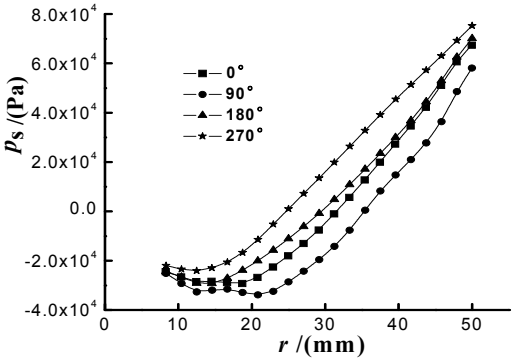

Figure 6. Static pressure distribution for the axial cross-section $Z = -10$ mm along the radial direction.

Figure 7 shows the static pressure distribution for the axial cross-section where Z is 12.5 mm, which is also based on the coordinate system in Figure 1. This axial section is the middle axial cross-section of the chamber. Figure 8 is generated according to the static pressure value and its position (radial direction). Figure 8 shows the static pressure p_s variable curves along the 0°, 90°, 180°, and 270° radial directions. Figures 7 and 8 show that the center of the chamber is the lowest pressure area in this axial cross-section, which is negative pressure (vacuum). So, the fluid flow from inlet to chamber can be formed.

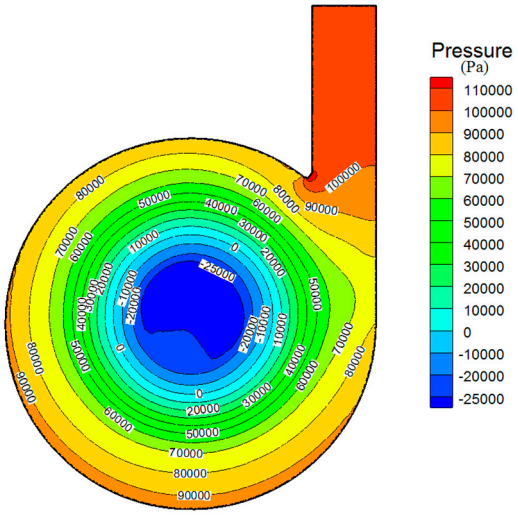

Figure 7. Static pressure distribution for the axial cross-section Z = 12.5 mm.

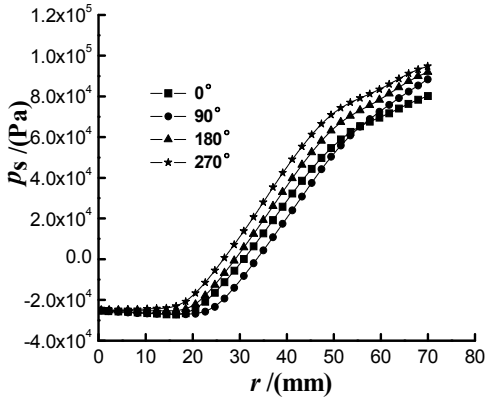

Figure 8. Static pressure distribution for the axial cross-section Z = 12.5 mm along the radial direction.

5.2. Flow Velocity Distribution in the Pump

Figures 9 and 10 are also the calculation result of CFX software. Based on the coordinate system in Figures 1, 9 and 10 respectively show the absolute velocity v, the circumferential velocity v_u, the radial velocity v_r, and the axial velocity v_z of two different axial cross-sections. Absolute velocity v is the vector synthesis result of v_u, v_r, v_z.

Figure 9 shows the velocity variable on the axial cross-section, where Z is -10 mm. This axial section is the middle cross-section of the impeller blade. Figure 9a–d show the v, v_u, v_r, v_z variable curves along the 0°, 90°, 180°, and 270° radial directions on the axial cross-section where Z is -10 mm.

Figure 10 shows the velocity variable on the axial cross-section, where Z is 12.5 mm. This axial section is the middle axial cross-section of the chamber. Figure 10a–d show how the v, v_u, v_r, v_z change along the 0°, 90°, 180°, and 270° radial directions on the axial cross-section, where Z is 12.5 mm.

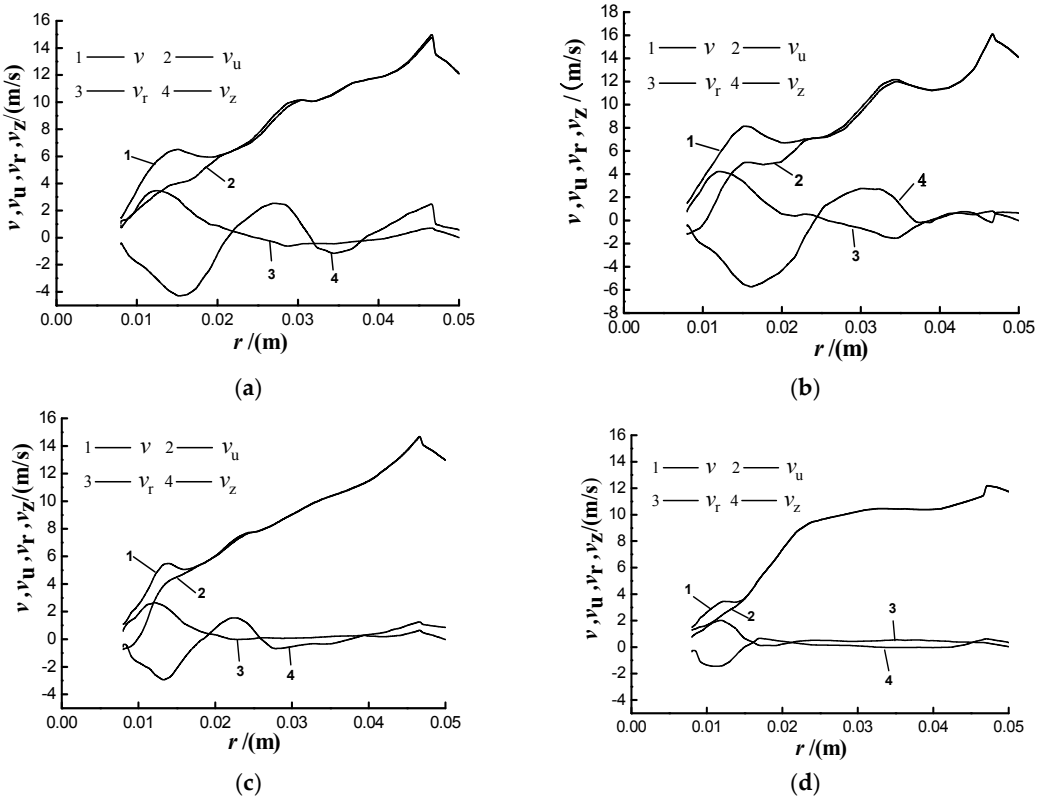

Figure 9. Velocity variable curves for the axial cross-section $Z = -10$ mm along the radial direction. (**a**) 0°; (**b**) 90°; (**c**) 180°; (**d**) 270°.

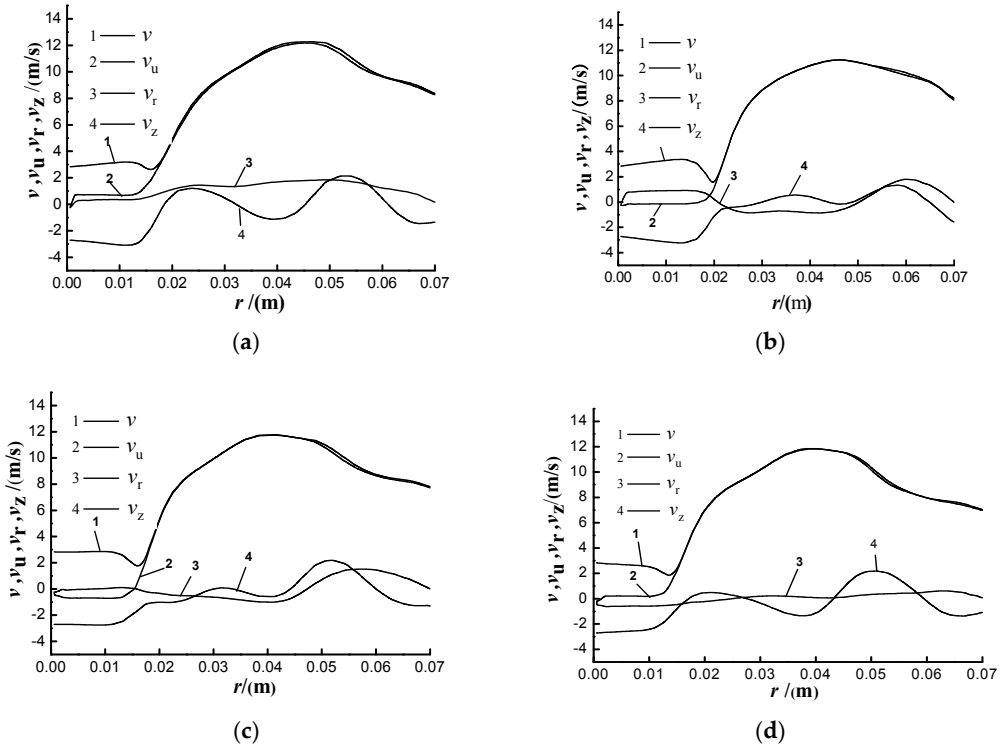

Figure 10. Velocity variable curves for the axial cross-section $Z = 12.5$ mm along the radial direction. (**a**) 0°; (**b**) 90°; (**c**) 180°; (**d**) 270°.

5.3. Numerical Simulation of the Pump Performance Curve

The discharge calculation software CFX was used to calculate the discharge at 2850 r/min. The calculated performance and measured curves are shown in Figure 11.

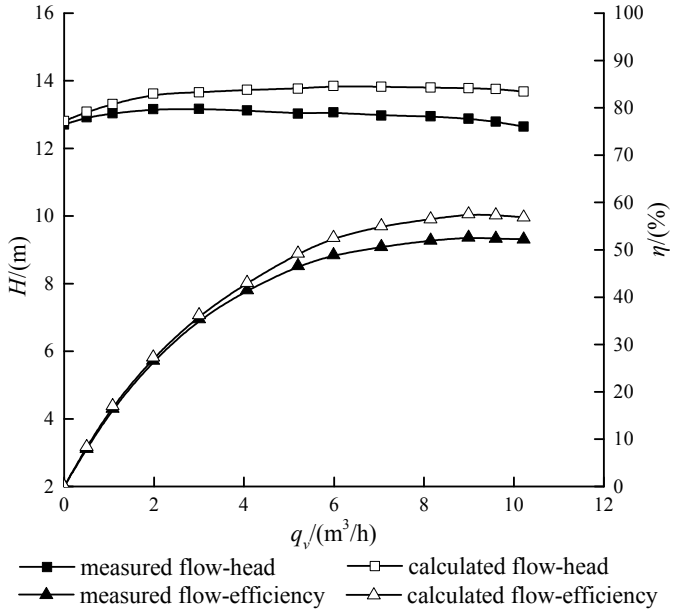

Figure 11. Performance comparison between experiments and simulation.

Disk frictional loss and volume loss are difficult to determine, and the computational fluid dynamics (CFD) numerical simulation pumper efficiency only considers hydraulic efficiency. The calculation model is simplified, for instance, by neglecting the clearance between the impeller back shroud, water pressure chamber, and surface roughness, etc.

6. Experimental Verification

In this paper, five spherical probes were used to extend into the vortex chamber, and five points were measured. The location of the measuring points is shown in Figure 12. The measuring system and principle of the probe are shown in Figure 11. The flow field calculation, measurement data, and the curve contrast are shown in Table 3 and Figure 13. Curves in Figure 13 are based on the coordinate system in Figure 1.

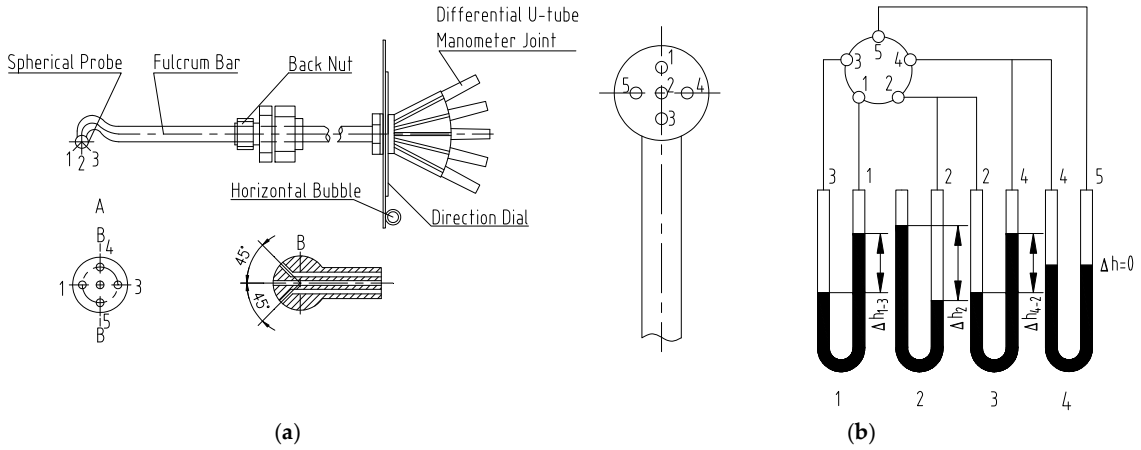

Figure 12. Probe measuring system. (**a**) Structure diagram of the five-hole spherical probe; (**b**) Connection system diagram of five-hole spherical probe and differential pressure meter.

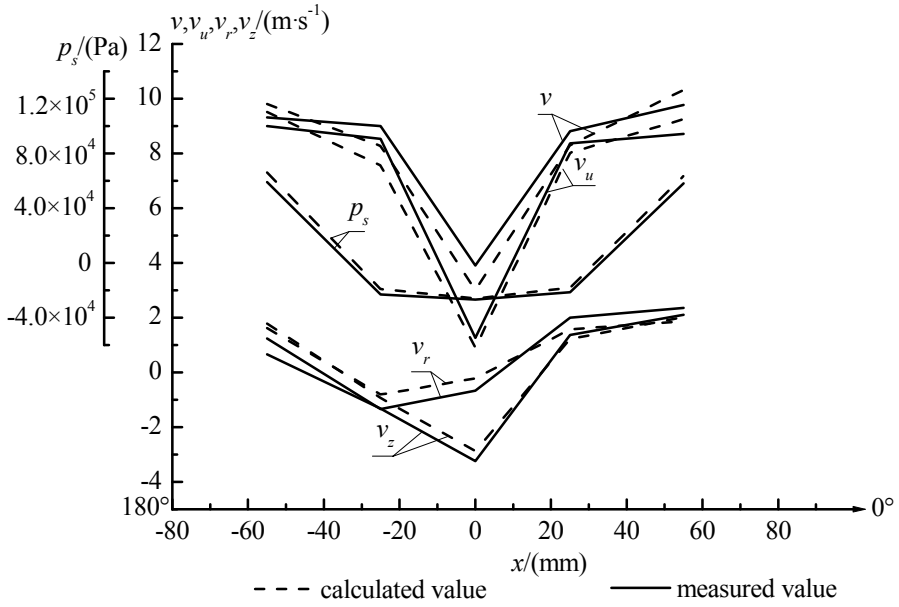

Figure 13. Calculated and measured curves of flow field curves on the axial-cross-section Z = 12.5 mm.

It can be seen from the comparison and analysis that the numerical calculation is consistent with the experimental results, which can reflect the internal flow pattern of the vortex pump. The numerical simulation results are reliable, and can be applied to the qualitative and quantitative analysis of the internal flow field of the vortex pump.

Table 3. Calculated and measured values of flow field curves on the axial cross-section Z = 12.5 mm.

Calculated and Measured Position	Discharge q_v/m^3·h^{-1}	Rotational Speed n/r·min^{-1}	Value Type	Absolute Velocity v/m·s^{-1}	Circumferential Velocity v_u/m·s^{-1}	Radial Velocity v_r/m·s^{-1}	Axial Velocity v_z/m·s^{-1}	Static Pressure p_s/Pa
x = −55 mm Measuring point a	9.31	2851	Calculated value	9.806	9.512	1.612	1.782	66,126
			Measured value	9.312	9.002	1.237	0.657	59,051
x = −25 mm Measuring point b	9.30	2851	Calculated value	8.267	7.567	−0.816	−0.939	−19,216
			Measured value	9.005	8.536	−1.341	−1.321	−23,064
x = 0 Measuring point c	9.32	2850	Calculated value	3.006	0.905	−0.223	−2.872	−26,138
			Measured value	3.902	1.264	−0.663	−3.242	−26,842
x = 25 mm Measuring point d	9.31	2849	Calculated value	8.306	8.026	1.572	1.216	−18,162
			Measured value	8.817	8.368	2.003	1.362	−21,447
x = 55 mm Measuring point e	9.31	2850	Calculated value	10.312	9.248	1.865	2.016	63,636
			Measured value	9.769	8.705	2.355	2.100	58,100

7. Comprehensive Analysis of Research Results

Based on the CFD numerical calculation and experimental results, we can carry out a comprehensive analysis of the internal flow rules of the vortex pump

Due to the unique structure and working principle of the vortex pump (i.e., the use of a semi-open impeller), the impeller and vortex chambers are fully open and connected, and the vortex chamber and pump outlet are connected through a channel. Carrying on with the flow field analysis, we must consider the concept of potential strength; i.e., the flow field of gravity and centrifugal inertia forces. The unequal mass force of the impeller is an important reason for the asymmetric distribution of the impeller flow field and the degree of disorder.

In the center of the impeller, because the hub occupies the central space, in order to form a vacuum range in the 10 mm < r < 20 mm annular area (r represents the radius with the center of the impeller as the origin), the lowest point of static pressure is in the upper y = 20 mm position, up to -3.6×10^4 Pa, and it can be inferred that bubbles are first produced in this region, while the lower static pressure remained at -2.7×10^4 Pa or so, forming clear dropped gradient upward pressure. The pressure in the lower half of the whole impeller chamber and the vortex chamber is greater than the pressure at the corresponding position of the upper part, and the static pressure reaches a maximum of about 1.1×10^5 Pa at the outlet of the pump body and becomes the main body of the pump head. The vacuum area is greater than the pump inlet area (pump inlet d = 32 mm). The main reason is the gravity field mass force potential function $W = gz$; the potential energy at the lower position is greater than that at the top. In addition, the lower gravity is in accordance with the centrifugal inertial force, increasing the pressure energy in the region. The structure is mainly due to the influence of the pump's outlet.

In the range of 20 mm < r < 48 mm, the static pressure of the impeller chamber and the vortex chamber grows linearly, which is influenced by the impeller and has a forced vortex property. In the range of 50 mm < r < 70 mm, the upward trend of static pressure is slowed down, which indicates that the imposition of the impeller is reduced and the steady growth of the static pressure is due to the increase in the volume of the vortex chamber and the partial kinetic energy. The hydraulic design of the radius of the volute chamber and the width of the channel is calculated by this principle, and the cross-sectional area of the flow passage is found in the determination of the optimum velocity in the flow passage.

In the range of r > 20 mm, the center speed of v_u and the absolute speed v of the impeller almost coincide with each other, and have greater values than the speed at the center of the vortex chamber. That is, the velocity of the volute chamber lags behind the rotation velocity of the impeller, and the vortex chamber v_u and v almost coincide. It can be seen that the width of the volute chamber should not be designed too wide under the premise of ensuring passing capacity; otherwise, the delay of the chamber velocity will increase.

Within the radius of the impeller, v_u is approximately equal to the circumferential velocity of the impeller with the same radius. The v_{umax} is approximately 14.3 m/s, which is equal to the circumferential velocity (v_u = 14.326 m/s) near the outer edge of the impeller. It can be shown that numerical simulation achieves sufficient accuracy. In the range of 20 mm < r < 48 mm, the center of v_u and v of the impeller rise almost linearly, and the center of the vortex chamber rises to approximately a parabola. In the range of r > 48 mm, the center of the vortex chamber is of approximately parabolic descent, and the partial kinetic energy is converted to pressure energy.

Because of the pressure gradient, the r < 20 mm v_z range of axial velocity distribution is not uniform, and the maximum velocity is in the position of 90° section y = 15 mm. At a maximum of about $v_{zmax} \approx 5.0$ m/s for the impeller, the volute chamber value is $v_{zmax} \approx 3.0$ m/s. In the r < 20 mm range, the radial velocity v_r varies irregularly, while in the r > 20 mm range, the radial velocity v_r fluctuates little.

The calculated pump head is slightly higher than the measured value. This is due to the neglect of mechanical loss and volumetric loss. The maximum hydraulic efficiency of the vortex pump is about 60%. Low hydraulic efficiency (i.e., flow loss) causes the main part of pump energy loss [20].

8. Conclusions

In a small flow state, the q_v-$NPSH_c$ curve of vortex pump is the opposite to the q_v-$NPSH_c$ of the centrifugal pump, and $NPSH_c$ value is large, that is, the vortex pump has poor anti-cavitation. At present, in ISO9906 (rotodynamic pumps—hydraulic performance acceptance tests—grades 1, 2 and 3), the evaluation methods of the centrifugal pumps are used for assessment of the rotodynamic pumps. Hence, the rationality of the evaluation methods is worthy of further study.

The experimental performance test of the prototype of the vortex pump (32WB8-12) indicates the 32WB8-12 pump has good performance and its optimized hydraulic model is worth popularizing. The numerical calculation is verified by the local experiment, and it is concluded that the numerical calculation of the internal flow field of the vortex pump gives realistic results. The pressure distribution in the vortex chamber presents a uniform increasing trend, and the velocity distribution appears to be in a turbulent state, which is characterized by a combined vortex. It is suggested that the flow rate be controlled to improve the efficiency of the vortex pump [21].

The stable pressure gradient is formed from the inlet of the vortex pump to the center of the impeller. The lowest pressure in the vortex chamber is -2.5×10^4 Pa and it is located at the center of the cavity of vortex chamber. The area of low pressure is greater than the pump entrance area. Therefore, the 32WB8-12 vortex pump has advanced suction and anti-cavitation performance.

Probes were used for measuring the pressure and velocity field synchronously, which had to be installed in the flow and caused slight interference to the original flow field and generated some error. In the following research, non-contact laser PIV technology will be applied to measure velocity, as it can obtain the velocity field accurately without disturbing the flow field. Non-contact laser PIV can be combined with the probe to measure the accurate internal flow field of the vortex pump. Furthermore, we will establish a flow model based on studies of precise numerical simulation technology and carry out studies on the two-phase flow medium and cavitation fluid field of the vortex pump. Thus, we can reveal the internal mechanism of the excellent performance of the vortex pump.

Author Contributions: The following statements should be used P.T. and Y.S. conceived and designed the experiments; D.T. and X.B. performed the experiments; X.B. and W.H. analyzed the data; J.M. and Y.F. contributed reagents/materials/analysis tools; P.T. and Y.S. wrote the paper.

Conflicts of Interest: The authors declare no conflict of interest.

References

1. Ohba, H.; Nakashima, Y.; Shiramoto, K. A Study on Internal Flow and Performance of a Vortex Pump Part 1: Theoretical Analysis. *Bull. JSME* **2008**, *26*, 999–1006. [CrossRef]
2. Schivley, G.P. An Analytical and Experimental Study of a Vortex Pump. *Trans. ASME Ser. D* **1970**, *92*, 889–900. [CrossRef]
3. Wen, Q.Y.; Guo, Y.H. Design of vortex pump for conveying potato. *Pump Technol.* **1998**, *2*, 25–26.
4. Chen, H.X. Measurement of rotating flow field within the impeller of vortex pump. *Trans. Chin. Soc. Agric. Mach.* **1996**, *27*, 49–54. (In Chinese)
5. Sha, Y.; Liu, X.S. Numerical calculation on gas-liquid two-phase hydrotransport and flow field measurement in volute with probes of a vortex pump. *Trans. Chin. Soc. Agric. Eng.* **2014**, *30*, 93–100.
6. Gerlach, A.; Thamsen, P.; Wulff, S.; Jacobsen, C. Design Parameters of Vortex Pumps: A Meta-Analysis of Experimental Studies. *Energies* **2017**, *10*, 58. [CrossRef]
7. Gerlach, A.; Thamsen, P.U.; Lykholt-Ustrup, F. Experimental investigation on the performance of a vortex pump using winglets. In Proceedings of the 16th International Symposium on Transport Phenomena and Dynamics of Rotating Machinery, Honolulu, HI, USA, 10–15 April 2016.
8. Gerlach, A.; Preuss, E.; Thamsen, P.U.; Lykholt-Ustrup, F. Numerical simulations of the internal flow pattern of a vortex pump compared to the Hamel-Oseen vortex. *J. Mech. Sci. Technol.* **2017**, *31*, 1711–1719. [CrossRef]
9. Jiang, D.L.; Lv, J.X.; Dai, L.; Su, B.W. A Numerical Simulation of and Experimental Research on Optimum Efficiency of Vortex Pump. *China Rural Water Hydropower* **2012**, *4*, 92–94, 98. (In Chinese)

10. Zhu, R.S.; Chen, J.J.; Wang, X.L.; Su, B.W. Numerical Simulation and Experimental of Influence of Hem and High-low Blade on Performance of Vortex Pump. *Flue Mach.* **2012**, *40*, 1–5.
11. Li, Y.; Zhu, Z.C.; He, W.Q.; Wang, Y.P.; Cui, B.L. Numerical Simulation and Experiment Analyses for the Gas-liquid Two-phase Vortex Pump. *J. Therm. Sci.* **2010**, *19*, 47–50. [CrossRef]
12. Xia, P.H.; Liu, S.H.; Wu, Y.L. Numerical simulation of steady flow in vortex pumps. *J. Eng. Thermophys.* **2006**, *27*, 420–422.
13. Shi, W.D.; Wang, Y.Z.; Kong, F.Y.; Sha, Y.; Yuan, H.Y. Numerical simulation of internal flow field within the volute of vortex pump. *Trans. Chin. Soc. Agric. Eng.* **2005**, *21*, 72–75.
14. Steinmann, A.; Wurm, H.; Otto, A. Numerical and experimental investigations of the unsteady cavitating flow in a vortex pump. In Proceedings of the 9th International Conference on Hydrodynamics, Shanghai, China, 11–15 October 2010.
15. Wei, Y.J.; Tseng, C.C.; Wang, G.Y. Turbulence and cavitation models for time-dependent turbulent cavitating flows. *Acta Mech. Sin.* **2011**, *27*, 473–487. [CrossRef]
16. Sha, Y.; Yang, M.G.; Kang, C.; Wang, J.F.; Chen, H.L. Design method and characteristic analysis of vortex pump. *Trans. Chin. Soc. Agric. Eng.* **2004**, *36*, 124–127.
17. Sha, Y.; Shi, W.D.; Wang, Z.L.; Ji, H.S. Hydraulic design of non-clogging pump and experimental research on its characters. *Trans. Chin. Soc. Agric. Mach.* **2005**, *36*, 62–66.
18. Chen, H.X. Research on Turbulent Flow within the Vortex Pump. *J. Hydrodyn. Ser. B* **2004**, *16*, 701–707.
19. Wu, J.; Sha, Y.; Xu, X. Experimental investigation on speed performance and volute flow of vortex pump. *J. Zhejiang Univ. Eng. Sci.* **2010**, *44*, 1811–1817.
20. Sha, Y.; Liu, X.S. Performance test on solid-liquid two-phase flow hydrotransport of vortex pump. *Trans. Chin. Soc. Agric. Eng.* **2013**, *29*, 76–82.
21. Quan, H.; Fu, B.H.; Li, R.N.; Zhang, T.; Han, W.; Li, J. Research Stage and Development Tendency of vortex pump. *Fluid Mach.* **2016**, *44*, 36–40.